Diamond & Related Materials 136 (2023) 110060

Contents lists available at ScienceDirect

Diamond & Related Materials

journal homepage: www.elsevier.com/locate/diamond

Study on a bifunctional switchable metasurface with perfect absorption and polarization conversion based on VO_2 and graphene in THz region

Xuejun Lian [a], Mengting Ma [a], Jinping Tian [a,b,*], Rongcao Yang [a]

[a] *College of Physics and Electronic Engineering, Shanxi University, Taiyuan 030006, China*
[b] *Computer Center, School of Modern Education Technology, Shanxi University, Taiyuan 030006, China*

ARTICLE INFO

Keywords:
VO_2
Graphene
Metasurface
Absorption
Polarization conversion

ABSTRACT

A switchable metamaterial device with dual function (SMDDF) based on vanadium dioxide (VO_2) and graphene is designed in this paper, where VO_2 is a phase change material and it can transition from the insulating state to the metallic state when it is stimulated by external conditions such as heat, electricity or light. In addition, graphene is a 2D active material and its conductivity can be well controlled by adjusting its bias voltage dependent chemical potential, which makes it have the advantage of easy integration. When VO_2 is in the metallic state and the chemical potential of graphene is set as 0.65 eV, the proposed SMDDF can behave as a single band absorber with the peak absorbance higher than 99.9 % at 1.8768 THz. However, when VO_2 is in the insulated state, and the chemical potential of the graphene pattern layer (GPL) is set as 0 eV, the proposed SMDDF will behave as a broadband linear polarization converter. It can convert the incident linearly polarized EM waves into the cross-polarized reflected waves within the frequency range of 2.12–3.58 THz, and the polarization conversion ratio (PCR) is >90 % with the relative bandwidth (W_{RB}) up to 51.23 %. Research results prove that the overall performances of the proposed bifunctional metamaterial device is superior to some of those reported in the literatures. Therefore, the research results of this paper may provide guidance for designing switchable multi-function terahertz devices using VO_2 and graphene in variable areas of practical applications.

1. Introduction

Terahertz (THz) waves are electromagnetic (EM) waves with frequencies from 0.1 to 10 THz (corresponding wavelengths from 3 mm to 0.03 mm) having many outstanding properties such as low energy, absorption, high transmittance and coherence. Metamaterials (MMs) are artificial electromagnetic materials that can exhibit properties that natural materials do not have. Due to the weak response of natural materials in the terahertz band, many functional MMs devices have been designed in THz band, such as superlenses [1,2], filters [3,4], perfect absorbers [5,6] and polarization converters [7,8]. Meanwhile, as a two-dimensional metamaterial with thickness very much smaller than the working wavelength, metasurface can also efficiently manipulate the THz waves [9,10] in the field of perfect absorbers [11], polarization converters [12], and so on. However, the earlier designed metamaterial devices based on metals have some drawbacks in practical applications since their properties are fixed once fabricated. Therefore, the dynamic control of terahertz waves by introducing some active materials [13–31] into the design of the metasurface has become one of the research directions in recent years. For example, Wang et al. proposed a three-band tunable perfect terahertz absorber based on liquid crystals [13]. Liu et al. designed a broadband metamaterial absorber based on graphene [14]. Yu et al. designed a reconfigurable metasurface by embedding photoconductive silicon [15]. Among the many types of active materials, phase change material (PCM) VO_2 is widely used in the design of tunable metasurfaces [18] because of its lower phase change temperature, ease of controlling and lower cost compared to GST [19,20]. In addition, graphene is another widely used 2D material, of which the carrier mobility and electrical conductivity can be adjusted by controlling the chemical potential through external gate voltage with lower ohmic loss than conventional metals [6,21] in the THz frequency range. In terms of the excellent properties of VO_2 and graphene, THz functional devices based on VO_2, graphene, and the combinations of VO_2 and graphene have been widely studied in recent years. For example, in 2020, Zhang et al. proposed a VO_2-based bifunctional multilayer metasurface capable of switching from an absorber to a reflective polarization converter [22], and then they designed a THz absorber with narrowband and broadband properties using graphene

---

[*] Corresponding author at: College of Physics and Electronic Engineering, Shanxi University, Taiyuan 030006, China.
E-mail address: tianjp@sxu.edu.cn (J. Tian).

https://doi.org/10.1016/j.diamond.2023.110060
Received 20 December 2022; Received in revised form 14 May 2023; Accepted 24 May 2023

and VO_2 [23]. In the same year, Song et al. proposed a switchable absorber between single band and broadband by using VO_2 [24]. In 2021, Liu et al. proposed a bifunctional metamaterial device based on a hybrid graphene and VO_2 configuration, which can realize a dynamic switch between beam steering and broadband absorption [25]. In 2022, the authors designed a broadband tunable THz metamaterial absorber (MA) in [26], where the top layer of the unit cell is composed of a graphene disk surrounded by a graphene square ring, the intermediate spacer layer is Rogers RT5880LZ, and the bottom layer is gold. Simulation results showed that the proposed structure can achieve an absorption rate above 90 % with a bandwidth of 2.173 THz (1.482–3.655 THz) and a fractional bandwidth ratio of 85 %. Also in 2022, Zhao et al. designed a metasurface based on VO_2 and graphene that enables reflective and transmissive polarization conversion [27], Zhou et al. designed a graphene-based reconfigurable metasurface to realize the mode switching of wavefront in THz band [28], He et al. proposed 4 THz graphene metasurfaces with wavefront control and polarization manipulation [29]. In 2023, Li et al. and Nie et al. proposed two VO_2-based metasurfaces that can achieve the state switching of THz wavefront [30] and the reconfiguration of THz wavefront [31], respectively. However, some of the metasurfaces mentioned above can only achieve the regulation between different frequency bands, while others can only use multi-layer structure or more than two metasurfaces to achieve different functions. These disadvantages will largely limit the practical application of the devices, and are also not easy to be controlled and fabricated. Therefore, it is necessary to create a compact metasurface with simple structure, ease of controlling and multiple functions.

To date, designs with simple structures that are functionally switchable between absorption and polarization conversion in the THz band have not been fully explored, although some studies have reported dual-control devices that combine metamaterials and the phase change material VO_2. In this paper, we propose a metasurface that can switch between dual functions through the phase transition of VO_2 and the change of Fermi energy level of graphene, which can then achieve single-band absorption as well as broadband cross-polarization conversion in the terahertz region. Note that the polyimide is chosen as the intermediate spacer layer, because it is a widely used dielectric material in the design of MM devices in THz frequency band, which is different from Ref. [26], where graphene-Rogers RT5880LZ-gold type sandwich structure is used to achieve broadband absorption in THz frequency band. When VO_2 is in the metallic state, and the Fermi energy level of graphene is set to 0.65 eV, the proposed SMDDF acts as a nearly perfect single-band MA with the absorbance over 99.9 % at 1.8768 THz. As a metamaterial device, the equivalent permittivity and permeability were also calculated. It is shown that the real part of equivalent permeability is always positive while the sign of the real part of the equivalent permittivity will change at 1.8768 THz, while the imaginary part of the equivalent permittivity is always positive. These all indicate that at this frequency, the reflection and transmission will be very small and the loss will be large, therefore, nearly perfect single band absorption effect is obtained. However, when VO_2 is in the insulated state, and the Fermi energy level of graphene is set to 0 eV, it will behave as a broadband linear polarization converter (LPC) with polarization conversion ratio (PCR) >90 % in the frequency range of 2.12–3.58 THz, and its relative bandwidth is 51.23 %. The proposed SMDDF can not only achieve both functions of absorption and polarization conversion based on actively adjustment of the VO_2 and graphene, but also has a relatively simple and compact structure. The excellent performance compared to those mentioned in the above references makes it possible to be applied in many broader application prospects, such as the fields of space light modulator, THz detection, stealth technology, and wireless communication.

2. Structure and design

Fig. 1(a) depicts the three-dimensional schematic diagram of our proposed SMDDF, the top view of a unit cell and the profile of graphene pattern are shown in Fig. 1(b) and (c), respectively. The top layer is a patterned gold resonator with VO_2 embedded in the two gaps (45° to the positive direction of y-axis) while the bottom layer is a gold plate. The middle part consists of two polyimide (PI) dielectric layers (with thickness t_3 and t_2) and a GPL sandwiched in between. The radius of the four circular holes in GPL is r and the center distance between two adjacent holes is k. In practice, the electrical conductivity of GPL can be regulated by an external electrical bias voltage V_g. In practical application, a thin polysilicon layer is often used as an electrode for regulating

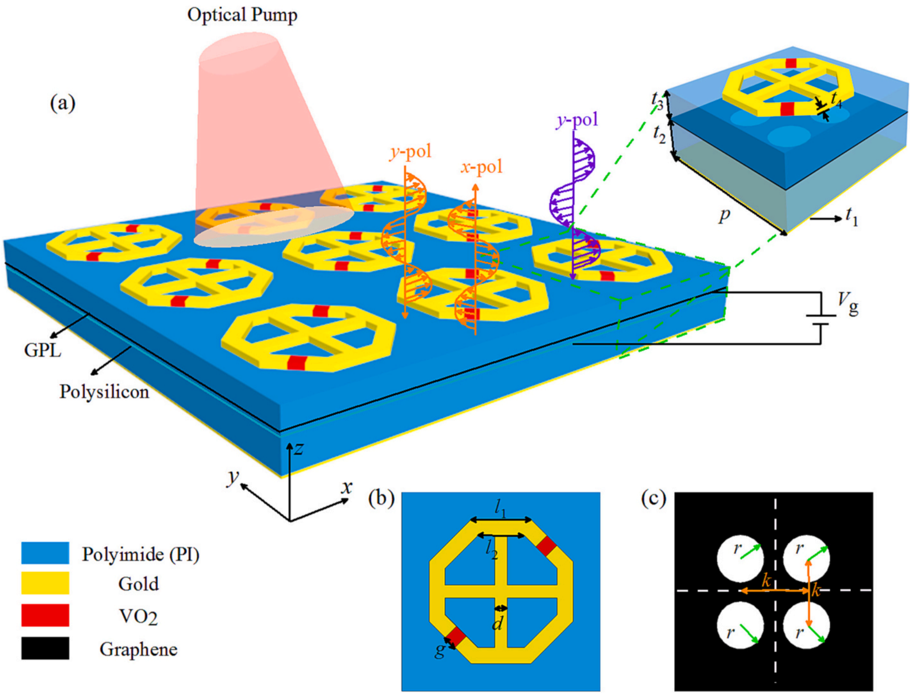

Fig. 1. (a) Schematic diagram of the SMDDF; (b) the top view of a unit cell; (c) the intermediate graphene pattern layer of a unit cell.

the chemical potential of graphene [32], because of its excellent semiconducting properties, as shown in Fig. 1(a). However, during numerical simulation, its effect on the overall performances can be neglected because it is extremely thin and transparent [23,32]. In addition, the properties of graphene will not be affected when the phase transition of VO_2 is excited by the pumping of visible light [33]. Meanwhile, when the proposed SMDDF works as a MA, the chemical potential of GPL is set to 0.65 eV to enhance the overall absorption by exciting the graphene surface plasmonic resonance (GSPR). But when it works as a LPC, the effect of GPL is also neglected by setting its chemical potential to 0 eV. The electrical conductivity of gold is 4.561×10^7 s/m [24], and the thickness bottom gold layer is $t_1 = 0.2\,\mu$m, which is thick enough to block the transmission of EM waves. The dielectric constant of PI is $\varepsilon_d = 3.5$ and the loss angle tangent is $tan\delta = 0.0027$ [34]. It is worth mentioning that PI material is chosen because of its lower thermal conductivity and relatively higher thermal stability [35]. After many times of numerical simulation, the optimized geometrical parameters of the proposed SMDDF are listed in Table 1 below. It is worth mentioning that when determining the thickness of the PI layer, we have made the following considerations. As a reflective MA, to achieve perfect absorption, the reflection must be suppressed. As a reflective LPC, to achieve perfect polarization conversion, we must suppress the reflection of co-polarized EM waves. Therefore, to determine the thickness of PI, it is necessary to make all the EM waves or the co-polarized EM waves propagate back and forth in the PI layer can be canceled through destructive interference. It is noting that during the process of determining the thickness of PI layer at the initial stage, the effect of GPL is also neglected for the aim of simplicity.

Within the THz frequency region, the relative permittivity of VO_2 can be described by the Drude model [36]:

$$\varepsilon_{VO_2}(\omega) = \varepsilon_\infty - \frac{\omega_p^2(\sigma)}{\omega^2 + j\gamma\omega} \tag{1}$$

where $\varepsilon_\infty = 12$ is the dielectric constant at infinite frequency, $\omega_p(\sigma)$ is the plasma frequency defined as $\omega_p^2(\sigma) = \frac{\sigma}{\sigma_0}\omega_p^2(\sigma_0)$ with $\sigma_0 = 3 \times 10^5$ S/m, $\omega_p(\sigma_0) = 1.4 \times 10^{15}$ rad/s, and $\gamma = 5.75 \times 10^{13}$ rad/s is the collision frequency. In this paper, the conductivity of VO_2 is set as 2×10^5 s/m when it is in metallic state, and is 0 s/m when it is in insulating state [37]. Furthermore, the graphene can be modeled as an equivalent 2D surface impedance layer without thickness, whose conductivity σ_g can be described by the Kubo equation [38]:

$$\sigma_g = \sigma_{intra} + \sigma_{inter} \tag{2}$$

$$\sigma_{intra} \approx \frac{ie^2Tk_B}{\pi\hbar^2(\omega + i\tau^{-1})}\left[\frac{\mu_c}{k_BT} + 2ln\left(exp\left(-\frac{\mu_c}{k_BT}\right) + 1\right)\right] \tag{3}$$

$$\sigma_{inter} = \frac{ie^2}{4\pi\hbar}ln\left[\frac{2|\mu_c| - (\omega + i/\tau)\hbar}{2|\mu_c| + (\omega + i/\tau)\hbar}\right] \tag{4}$$

where μ_c is the chemical potential, and e, k_B, $\hbar$ are the charge of the electron, the Boltzmann constant, and the reduced Planck constant, respectively. $T = 300$ K is the temperature, and τ is the relaxation time. The numerical simulations are carried out in the frequency domain using the EM simulation software CST, which is based on the finite integration technique. During the simulation, unit cell boundary conditions are set along the x- and y-axis directions and open boundaries are set along the z-axis direction. The whole structure is illuminated by a y-polarized plane wave propagating along the -z direction unless otherwise stated due to the C2 symmetry of the structure.

Table 1
Optimized geometrical parameters of the proposed SMDDF.

Parameters	Symbol	Optimized value (μm)
Period of a unit cell	p	30
Thickness of the bottom gold layer	t_1	0.2
Thickness of the lower PI dielectric layer	t_2	4.9
Thickness of the upper PI dielectric layer	t_3	4
Thickness of the gold-VO_2 pattern layer	t_4	0.8
Outer edge length of the gold pattern	l_1	9
Inner edge length of the gold pattern	l_2	7
Arm width of the inner gold cross	d	1.9
Gap width where VO_2 is embedded	g	2.1
Radius of circular holes in graphene	r	3.6
Center distance between two adjacent holes	k	10

The equivalent circuit of the proposed SMDDF is shown in Fig. 2. For the LPC mode, as shown in Fig. 2(a), GPL is neglected. The topmost layer can be equivalent to a series RLC circuit, the PI layer can be seen as a segment of transmission line with impedance Z_{PI}, and the gold ground can be seen as a short circuit. $Z_0 \approx 377\Omega$ is the free space impedance and Z_{in} represents the equivalent input impedance of the SMDDF. For the MA mode, as shown in Fig. 2(b), the topmost layer and the GPL can be respectively equivalent to two separate series RLC circuits. In addition, the two layers of PI above and below graphene are equivalent to two transmission lines with different lengths. $Z_{in}^{'}$ represents the overall equivalent impedance. Therefore, the resonant frequency of the designed SMDDF for the two modes can be qualitatively obtained based on the formula:

$$f = \frac{1}{2\pi\sqrt{L_{eff}C_{eff}}} \tag{5}$$

where, L_{eff} and C_{eff} represent the equivalent inductance and capacitance in the two modes, which can be derivate after some algebraic derivation. To be noted is that the more detailed expressions or equations of the equivalent circuit is not shown because of the complex derivation processes and in this paper, we only need to qualitatively analyze the simulation results based on the simplified equivalent circuit.

A possible fabrication process for the proposed structure can be briefly described as follows: i) a 0.2-μm-thick gold reflection layer is grown on a sufficiently thick silicon substrate using electron-beam evaporation method; ii) a layer of PI dielectric is deposited on top of the gold layer by means of a spin coating and curing process; iii) continuous graphene film growth on PI by chemical vapor deposition (CVD), and GPL by electron beam lithography and reactive ion etching; iv) another layer of PI dielectric is deposited; v) a 0.8-μm gold film is deposited, and then it is patterned using photolithography [34]; vi) VO_2 is then deposited using magnetron sputtering and the lift-off craftsmanship; and vii) finally the whole structure is stripped from the silicon substrate [34,38–40].

3. Results and analysis

3.1. Function of perfect absorbing

When the proposed SMDDF is pumped by a beam with a certain power, phase transition of VO_2 will happen and it will exhibit the similar properties to those of metals. At the same time, the chemical potential of graphene can be set to 0.65 eV by applying an external gate voltage. Consequently, the whole structure will act as a typical MA. The absorbance can be expressed as $A = 1 - R - T$, where $R = |r_{yy}|^2 + |r_{xy}|^2$ is the

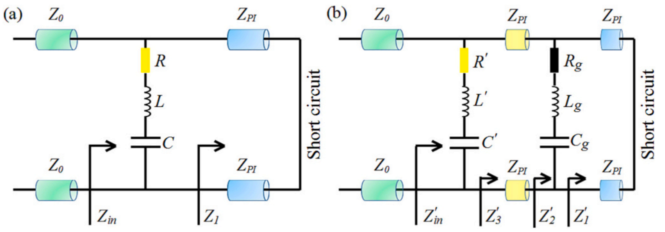

Fig. 2. Equivalent circuit model: (a) LPC mode, (b) MA mode.

total reflectance, and the total transmittance can be written as $T = \left|t_{yy}\right|^2 + \left|t_{xy}\right|^2$. To be noted is that co- and cross-polarized reflection and transmission are both considered in order to make the calculation results more accurate. The second subscript represents the polarization of incident EM waves while the first one represents the polarization of reflected and transmitted EM waves. The total transmission has been designed to $T = 0$ in this paper and the total absorptivity can be simplified to $A = 1 - \left|r_{yy}\right|^2 - \left|r_{xy}\right|^2$ [40,41]. The well-known impedance matching theory can be used to elaborate the background physical mechanism of a MA. The effective surface impedance $Z(f)$ relative to the vacuum of a designed MA can be calculated according to $Z(f) = \sqrt{\frac{\mu_{eff}}{\varepsilon_{eff}}} = \sqrt{\frac{(1+S_{11})^2 - S_{21}^2}{(1-S_{11})^2 - S_{21}^2}}$ [14]. It is obvious that $Z(f) = 1$ will be satisfied if the scattering parameters S_{21} and S_{11} are both zero, which means the perfect impedance matching between the free space and the proposed SMDDF, then we will have $\mu_{eff} = \varepsilon_{eff}$.

The simulated absorbance, transmittance and reflectance are shown in Fig. 3(a), from which one can find that when the EM wave is incident normally, the proposed SMDDF shows good performance of single-band perfect absorption in the frequency range of 1.5–2.3 THz with a near 100 % absorption peak located at 1.8768 THz. Fig. 3(b) demonstrates the calculated real and imaginary part of $Z(f)$, from which it can be found that the real part of $Z(f)$ is close to 1 and the imaginary part is close to 0 at the frequency of 1.8768 THz. Therefore, the impedance matching condition between the free space and the proposed ideal absorber is nearly achieved, resulting the nearly perfect single-band absorption at this frequency. In addition, simulations have shown that when the proposed SMDDF is operated as a MA, the GPL can not only enhance the overall absorption, but also can be used to dynamically adjust its central frequency or absorption intensity. As shown in Fig. 3(c), with the increase of the graphene chemical potential μ_c from 0.45 eV to 0.85 eV, the absorbance increases first and then decreases. Meanwhile, the absorption spectrum is blueshifted, which has the potential of being used as a switching. For example, at around 1.75 THz, two states of "ON" and "OFF" can be defined because the absorption is >95 % and <30 % when the graphene chemical potential is 0.55 eV and 0.85 eV, respectively. And at around 2.04 THz, the opposite phenomena is exhibited. Furthermore, as shown in Fig. 3(d), it is found that the change of graphene relaxation time τ has some weak effect on the absorption intensity, while has almost no effect on the position of the absorption peak. Moreover, as a type of metamaterial device, it is necessary to discuss the equivalent permittivity and permeability. Fig. 3(e) and (f) shows the retrieved real and imaginary part of these two equivalent constitutive parameters. It is obvious that the real part of equivalent permeability is always positive while the real part of equivalent permittivity crosses the x-axis at the frequency corresponding the absorption peak, which means the excitation of electric resonance. Meanwhile, at the frequency of the absorption peak, both the real and imaginary part of the equivalent permittivity and permeability are equal, proving once again the nearly perfect impedance matching and near unity absorption.

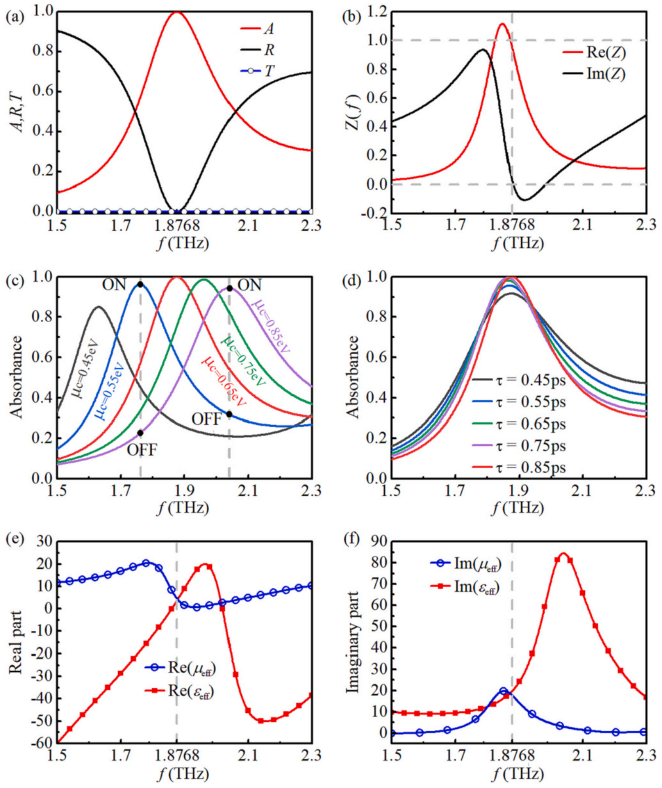

Fig. 3. (a) Spectral curves of absorbance (red), reflectance (black) and transmittance (blue), (b) real (red) and imaginary (black) parts of the effective surface impedance, (c) absorbance with different graphene chemical potentials and (d) absorbance with different graphene relaxation times, (e) real part of the equivalent permittivity (red) and permeability (blue), (f) imaginary part of the equivalent permittivity (red) and permeability (blue). (For interpretation of the references to color in this figure legend, the reader is referred to the web version of this article.)

In order to gain more insight into the physical mechanism of absorption, we also studied the distribution of electric field, surface current of the proposed SMDDF at the center frequency 1.8768 THz. Fig. 4(a), (b) and (c) shows the distribution of surface current on the top pattern layer, on the GPL and on the bottom gold plate, respectively. It is obvious that, the induced surface currents on the top layer are much stronger than those on the GPL and the bottom gold plate, which indicates again the absorption is dominated by the excitation of electric resonance. It is the combined action of electric and magnetic resonances that result in the perfect absorption. The corresponding distribution of electric field component E_z on the three layers is shown in Fig. 4(d), (e) and (f), indicating the excitation of electric dipole resonance along the top gold pattern, the local surface plasmon resonance (LSPR) along the graphene, and the weaker propagating plasmon resonance (PSPR) along the bottom gold plate. These types of resonant electric fields which will couple strongly with the incident electric fields, trapping the incident electromagnetic fields into the proposed absorber to form perfect absorption.

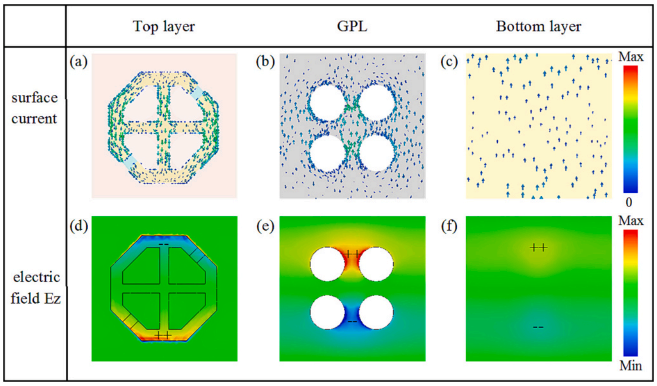

Fig. 4. Upper panel: distribution of the induced surface current on (a) the top pattern layer and (b) the GPL, (c) the gold bottom plate. Lower panel: distribution of the induced electric field component E_z on the corresponding layers. (For interpretation of the references to color in this figure legend, the reader is referred to the web version of this article.)

3.2. Function of polarization conversion

When VO_2 is in the insulating state and the Fermi energy level of GPL is set to 0 eV, both the effect of VO_2 and GPL on the property of the proposed SMDDF can be neglected [40]. As a result, the overall structure becomes anisotropy, and which will make the proposed SMDDF behave as a reflective LPC. We can use the eigenmode decomposition to explain the working mechanism of the polarization conversion, as shown in Fig. 5(a). We first decompose the incident electric field E_i into two orthogonal components E_{iu} and E_{iv} along the u and v axes. Then the electric field component of the incident EM wave can be expressed as $\overrightarrow{E}_i = \overrightarrow{u}E_{iu} + \overrightarrow{v}E_{iv}$, and the corresponding reflected electric field can be written as $\overrightarrow{E}_r = \overrightarrow{u}r_{uu}E_{iu} + \overrightarrow{v}r_{vv}E_{iv}$, where r_{uu} and r_{vv} are the reflection coefficients along the u-axis and v-axis, respectively. Because of the anisotropy of the metasurface, the amplitude $r_{uu}(r_{vv})$ and the phase $\phi_{uu}(\phi_{vv})$ of the two orthogonal reflection components will change when the polarized EM wave illuminates the SMDDF normally. When $|r_{uu}| \approx |r_{vv}|$ and $\Delta\phi = \phi_{uu} - \phi_{vv} = \pm 180^{\circ}$, the synthesis direction of E_{ru} and E_{rv} will be along the x-axis direction, namely, the incident y-polarized wave will be converted to the reflected x-polarized wave. In other words, cross polarization conversion of linearly polarized EM wave is achieved. Fig. 5(b) shows the reflection amplitude as well as the phase difference when the incident EM wave is polarized along the u-axis and v-axis, respectively. It can be found that in a wide frequency range, the amplitudes of r_{uu} and r_{vv} are almost equal and the phase difference $\Delta\phi$ is about 180°, which agrees with the above theoretical prediction, indicating a better function of linear polarization conversion.

Fig. 5(c) shows the co-polarization reflection coefficient r_{yy} and cross-polarization reflection coefficient r_{xy}, from which one can find that r_{yy} is lower than 20 % while r_{xy} is >90 % in a wide frequency range of interest. Especially, there are three reflection dips in the spectral line of co-polarization coefficient r_{yy}, indicating that most of the reflected wave is the x-polarized component. In terms of the symmetry of the structure, similar results will be obtained for the x-polarized incident EM waves. To further study the polarization conversion capability of the proposed SMDDF, the polarization conversion ratio (PCR) is calculated from the following formula [12]:

$$\mathrm{PCR} = \frac{|\mathrm{r_{xy}}|^2}{|\mathrm{r_{xy}}|^2 + |\mathrm{r_{yy}}|^2} \tag{6}$$

As shown in Fig. 5(d), the PCR is >90 % in the frequency range of 2.12–3.58 THz, and it will close to 100 % at the three resonance frequencies of $f_1 = 2.22$ THz, $f_2 = 2.59$ THz, and $f_3 = 3.34$ THz, respectively. In practical applications, broadband polarization converters are favored, for which the relative bandwidth (W_{RB}) is a key criterion, and it can be estimated between the lowest frequency f_{min} and the highest frequency f_{max} limited by the desired PCR in terms of $W_{RB} = \frac{2\times(f_{max}-f_{min})}{f_{max}+f_{min}}$ [42]. The calculated W_{RB} is close to 51.23 %, indicating a broadband conversion property. Meanwhile, it is well-known that the multi-reflection interference theory (MRIT) can be used to check the correctness of the simulation results and to interpret the background physical mechanism of the polarization conversion [43,44]. The calculated results using MRIT are also shown in Fig. 5(c), which agree well with the simulation results, indicating the correctness of our simulations.

Furthermore, the polarization properties of EM waves can be described by the polarization azimuth angle φ and ellipticity χ [45]:

$$\varphi = \frac{1}{2}tan^{-1}\left(\frac{2kcos(\phi)}{1-k^2}\right) \tag{7}$$

$$\chi = \frac{1}{2}sin^{-1}\left(\frac{2ksin(\phi)}{1+k^2}\right) \tag{8}$$

where $k = |r_{xy}|/|r_{yy}|$, ϕ represents the phase difference between the cross- and co-polarization reflection coefficients. The parameter φ represents the rotation angle of the reflected EM wave with respect to the incident one, while χ denotes the polarization state of the reflected EM wave. If $\chi = 0^{\circ}$, it means that the reflected wave is still a linear polarization EM wave, otherwise it is in other polarization states. If $\chi = 0^{\circ}$ and $\varphi = 90^{\circ}$, it indicates that the y-polarized wave can be converted to x-polarized wave. In addition, polarization extinction ratio (PER) [46] is also a key parameter used to weigh the polarization conversion ability:

$$PER = 10 \times log\left(|r_{xy}|^2 / |r_{yy}|^2\right) \tag{9}$$

Besides, as a reflective LPC, it not only requires higher PCR, but also needs to make better use of EM wave energy. Therefore, the energy absorbance and the energy conversion ratio are also considered, which can be defined as $A = 1 - |r_{xy}|^2 - |r_{yy}|^2$ and $ECR = |r_{xy}|^2 + |r_{yy}|^2$ [46,47], respectively. As shown in Fig. 6(a) and (b), we can see clearly that the polarization azimuth angle φ is about 90° in the frequency range of 2.12–3.58 THz, and the corresponding ellipticity χ is close to 0°, which means that the reflected wave is still a linearly polarized EM wave but is rotated by 90° with respect to the incident wave. These results again verify the effectiveness of our design in the function of polarization conversion. As shown in Fig. 6(c), the PER is >22 dB in the frequency range of interest, which indicates the better extinction performance and the potential application prospects. In addition, as indicated in Fig. 6(d), the energy absorbance is below 21.8 % in the frequency range of high efficiency polarization conversion, and the energy conversion ratio ECR is >90 %, which represents that the proposed SMDDF can reflect almost all of the incident EM waves without excessive losses and has a higher efficiency of energy utilization.

In purpose to better elucidate the physical mechanism of the polarization conversion, we discuss the distribution of surface currents. As shown in Fig. 7(a), for the incident y-polarized EM waves at frequency of $f_1 = 2.22$ THz, the currents on the left upper arm and right lower arm of the gold pattern flows in the opposite direction to those on the bottom metal plate, it will excite an induced magnetic field $\mathrm{H_1}$. As shown in Fig. 7(b), $\mathrm{H_1}$ can be decomposed into two orthogonal components $\mathrm{H_{1x}}$ and $\mathrm{H_{1y}}$. Because the component $\mathrm{H_{1y}}$ is parallel to the incident electric

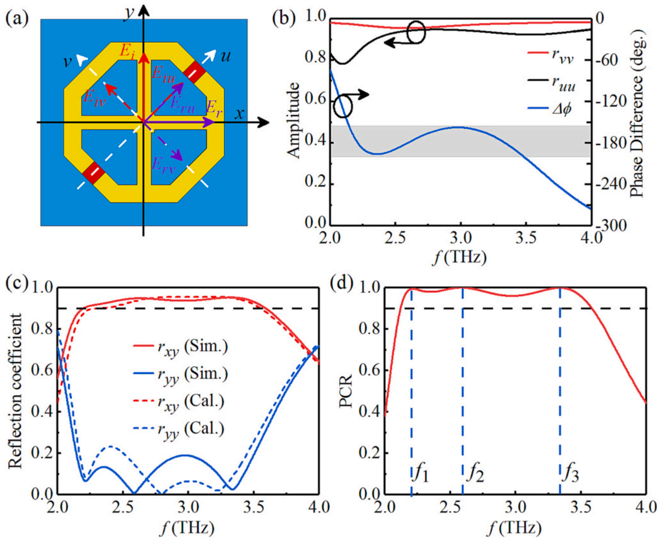

Fig. 5. (a) Diagram of eigenmode decomposition, (b) amplitude and phase difference of the reflection for u- and v-polarized EM wave, (c) simulated (solid) and calculated (dashed) amplitude of two orthogonal reflected waves polarized along the x-axis and y-axis when the incident EM wave is polarized along y-axis, and (d) polarization conversion ratio (PCR).

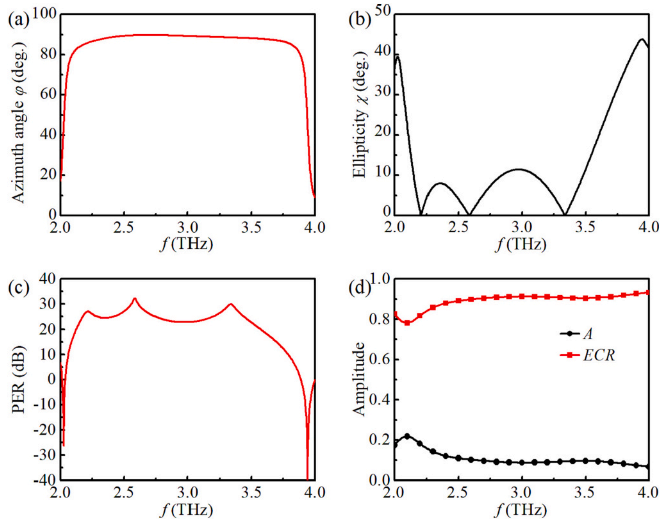

Fig. 6. Dependence of (a) polarization azimuth angle φ, (b) ellipticity χ, (c) polarization extinction ratio *PER*, and (d) energy absorbance *A* and energy conversion ratio *ECR* on the operating frequency.

field E_{iy}, the cross-coupling between them will lead to the conversion from incident *y*-polarization waves to reflective *x*-polarization waves. However, the component H_{1x} is parallel to the incident magnetic field H_{ix}, it cannot generate cross-polarized waves. In addition, the induced current on the center cross-shaped part of the gold pattern can excite electric resonance to generate the induced electric field E_1. By decomposing E_1 into orthogonal components E_{1x} and E_{1y}, we can find that the component E_{1x} is perpendicular to the incident electric field E_{iy}, which can further enhance the polarization conversion. In terms of the similar mechanisms, as depicted in Fig. 7(c)–(f), cross-polarization conversion at $f_2 = 2.59$ THz and $f_3 = 3.34$ THz can be well interpreted. In brief, it is the electric and magnetic resonances that act together to form the broadband cross-polarization conversion.

4. Parameter dependency of the proposed SMDDF

Geometric tolerances introduced by the actual processing of the device are unavoidable, thus it is essential for us to study the effects of small changes of some key structural parameters on the performance of the proposed SMDDF. As shown in Fig. 8(a) and (b), the slight change of the radius *r* of the circular holes on the graphene and the slight change of the center distance of the two adjacent circles *k* will not bring obvious changes in the overall absorption property. Therefore, the use of GPL can effectively improve the overall absorption performance, but some slight changes in the shape of the pattern of GPL can hardly change the overall performance.

We next discuss the effects of parameters l_1, l_2 and *p* on the separate performance. From Fig. 9(a)–(d), it can be seen that as l_1 changes from 8.90 μm to 9.10 μm or l_2 varies from 6.8 μm to 7.2 μm, the performance is basically stable no matter the proposed SMDDF is operated as a MA or as a LPC. The negligible slight shift of the spectral lines can be explained

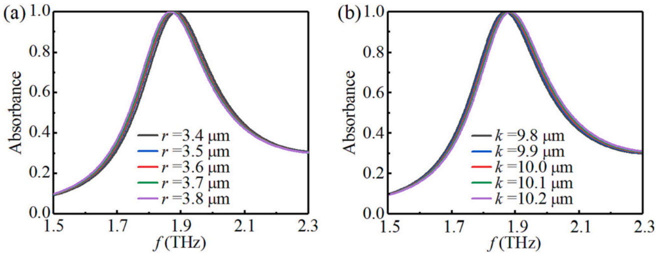

Fig. 8. Effect of parameters *r* and *k* on absorption (a, b) performance.

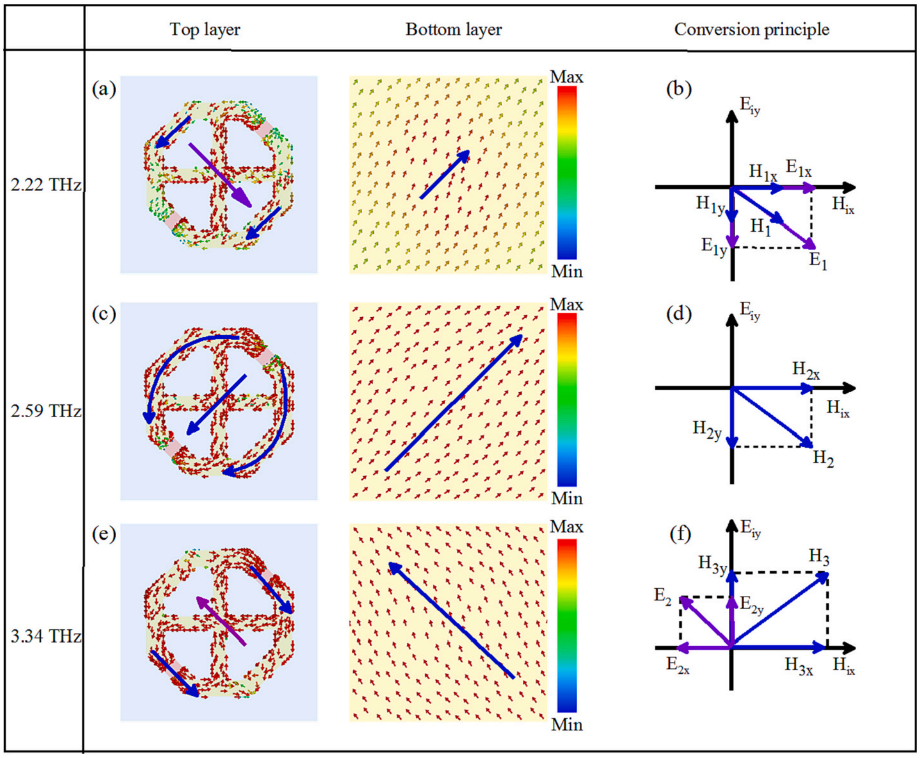

Fig. 7. Distribution of the surface current along the top layer and the gold bottom plate under the normal incidence of *y*-polarized wave: (a) $f_1 = 2.22$ THz, (c) $f_2 = 2.59$ THz, (e) $f_3 = 3.34$ THz; (b), (d) and (f) are respectively the corresponding polarization conversion principle. (For interpretation of the references to color in this figure legend, the reader is referred to the web version of this article.)

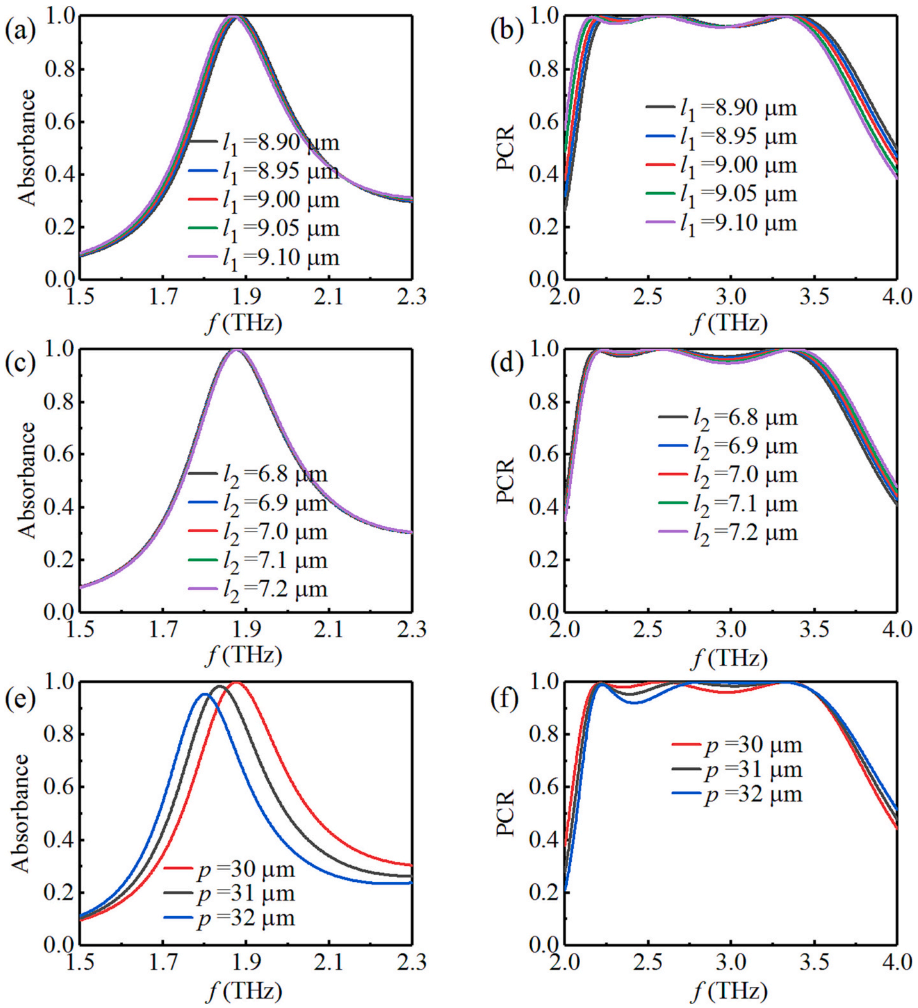

Fig. 9. Effect of parameters l_1, l_2 and p on the performance of absorption (a, c, e) and polarization conversion (b, d, f).

by the distribution of electric fields and surface currents discussed above. However, as indicated in Fig. 9(e), when the proposed SMDDF is operated as a MA, with the increase of parameter p from 30 μm to 32 μm, the absorption peak will have an obvious redshift together with the decrease of absorption intensity due to impedance mismatch. If it is operated as a LPC, as shown in Fig. 9(f), the increase of parameter p has almost no clear effect on the overall PCR band. Based on these results, we choose $l_1 = 9\ \mu m, l_2 = 7\ \mu m$ and $p = 30\ \mu m$ as the optimized values.

The effects of parameters d and g have also been studied. As shown in Fig. 10(a) and (c), when these two parameters are changed, the absorption spectra remain unchanged. It is because that, as shown in Fig. 4, the electric field is mainly distributed on the upper and lower sides of the gold-VO_2 pattern, which is not dependent on the above two parameters. However, they will clearly affect the PCR spectra when the proposed SMDDF is operated as a LPC, as shown in Fig. 10(b) and (d). On the one hand, this can be well interpreted from the distribution of surface currents shown in Fig. 7. On the other hand, increasing d means the decrease of equivalent inductance originated from the gold strips and increasing g means the decrease of equivalent capacitance originated from the two gaps embedded with VO_2. Therefore, according to $f = 1/(2\pi\sqrt{L_{eff}C_{eff}})$, the spectral lines of PCR will move towards higher frequency [12]. As a result, we select $d = 1.9\ \mu m$ and $g = 2.1\ \mu m$ as the optimal values. Finally, we discuss the effects of the thickness of upper dielectric layer t_3 on the device performance. As shown in Fig. 10(e), with the variation of t_3 from 3.8 μm to 4.2 μm with a step of 0.1 μm, there is a slight blueshift in the absorption spectra. It is because that, with the increase of the spacing between the top gold-VO_2 pattern layer and the GPL, the equivalent capacitance between the top and bottom plate of the structure will be decreased, thus leading to the slight blueshift of absorption spectrum to higher frequency. However, when the proposed SMDDF is operated as a LPC, the PCR spectrum shows a slight narrowing trend, which is easy to be understand. In this case, the effect of graphene can be neglected because its chemical potential is 0 eV. Then the increase of t_3 is the same as the increase of t_2 or $t_3 + t_2$, which means the increase of the overall thickness of the dielectric layers. As a result, it will lead to the increase of the accumulated phase and optical path when it propagates in the dielectric layer. As a result, it will reduce the resonance frequency of the excited magnetic resonances and lead to the redshift of the right two PCR peaks.

It is well-known that for a MA, polarization insensitivity and wide incident angle characteristics are preferred. Fig. 11(a) and (b) depict the dependence of the absorbance on the polarization angle and the incident angle of the y-polarized incident EM wave, respectively. It can be obviously seen that the absorbance is insensitive to the change of polarization angles because of the rotational symmetry of the structure. Meanwhile, it can also keep at higher absorbance until the incident angle is larger than 60°, indicating better property of wide incident angle. Furthermore, when VO_2 is in insulating state, the proposed SMDDF will be operated as a LPC. It can be seen from Fig. 11(c) that when the polarization angle increases from 0° to 45° and then to 90°, the PCR will change from nearly 100 % to 0 and then to nearly 100 % due to the symmetry of the structure. From Fig. 11(d), it can be found that the intensity and bandwidth of PCR remain almost unchanged when the

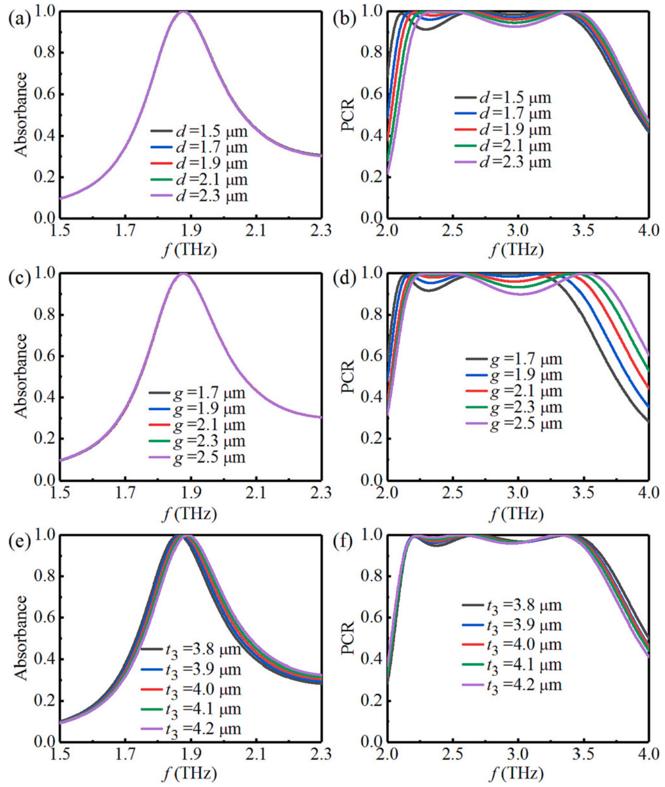

Fig. 10. Effect of parameters d, g and t_3 on absorption (a, c, e) and polarization conversion (b, d, f) performance.

incident angle is increased from 0° to 15°. As the incidence angle continues to increase, the PCR spectrum will gradually split due to the appearance of parasitic additional resonance and the increase of diffraction effect [44].

In Table 2, we compared the results of this paper with the recent reported researches to highlight the advantages and the novelty of the proposed SMDDF. It shows that if the difficulty and cost of device fabrication, the use of tunable materials, the unit cell size, the operating bandwidth, the perfect absorption, and the high polarization conversion efficiency are comprehensively considered, the SMDDF designed in this paper is superior to those in the reported literatures. Therefore, the proposed SMDDF can achieve dual functions of MA and LPC with smaller cell size, higher absorbance/wider polarization conversion bandwidth, and fewer structure layers, thus can facilitate the practical applications.

5. Conclusion

In summary, we propose a bifunctional switchable metasurface based on vanadium dioxide and graphene. By changing the state of vanadium dioxide and controlling the chemical potential of graphene, flexible switching of operating modes of absorption and cross-polarization conversion can be achieved in the terahertz band. We theoretically analyzed the principles of the working mechanism of the two functions by simulating the distribution of surface currents and electric fields, as well as the eigenmode decomposition. When VO_2 is in the metallic state and the graphene chemical potential is set as 0.65 eV, the proposed SMDDF behaves as a narrowband absorber with the peak absorption >99.9 % at the resonant frequency of 1.8768 THz. When VO_2 is in the insulated state and the chemical potential of graphene is set to 0 eV, the proposed SMDDF can achieve a broadband cross-polarization conversion in the range of 2.12–3.58 THz with a relative bandwidth of 51.23 %. Then MRIT was applied to verify the correctness of the simulation results. Furthermore, we discussed the effect of the geometric

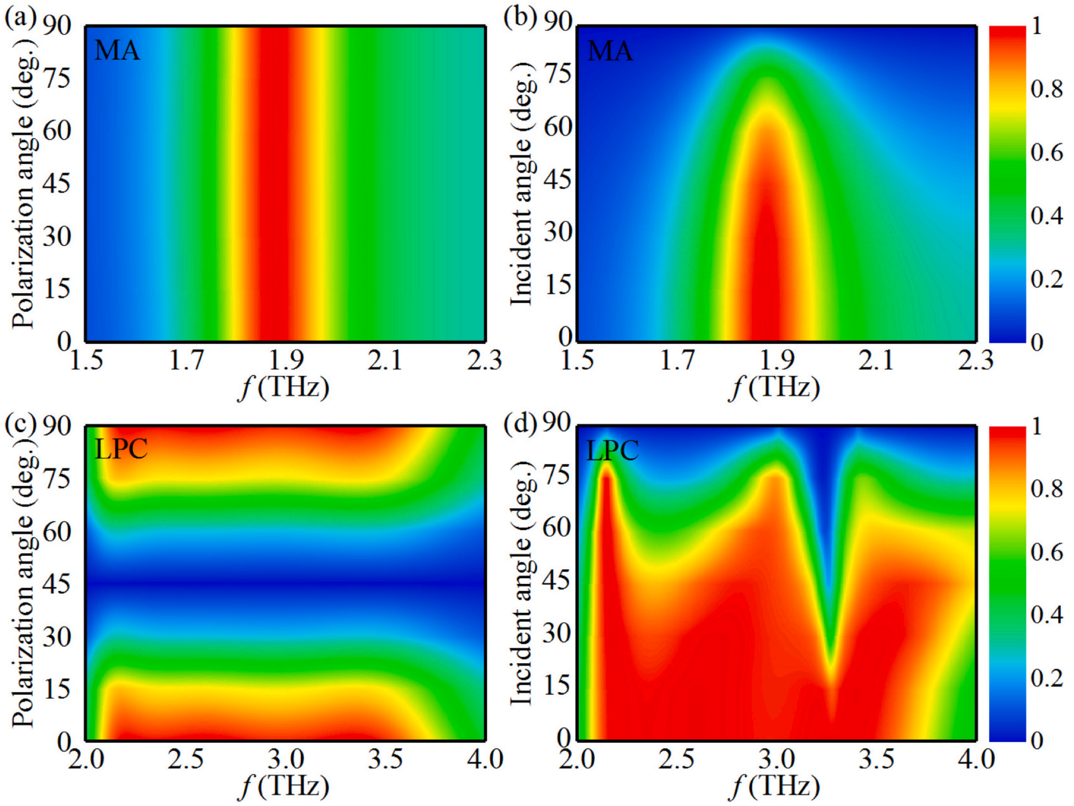

Fig. 11. Effect of (a) polarization angle and (b) incidence angle on the absorbance when the proposed SMDDF is operated as a MA with VO_2 in the metallic state and $\mu_c = 0.65$ eV; (c) and (d) are the corresponding cases of PCR when the proposed SMDDF is operated as a LPC with VO_2 in the insulating state and $\mu_c = 0$ eV.

Table 2
Comparison with recent reported multifunctional metasurfaces.

Refs.	Functions	Results		Cell size (μm)	Materials	Layers
		Frequency (THz)	A/PCR			
[24]	Abs	0.677	>90 %	200	VO_2	6
	Abs	0.393–0.897	>90 %			
[23]	Abs	1.37	≈100 %	40	Graphene & VO_2	5
	Abs	1.05–2.35	>90 %			
[22]	Abs	2.5	>90 %	40	VO_2	6
	PC	2–3	>90 %			
[42]	Abs	0.52–1.20	>90 %	150	VO_2	6
	PC	0.42–1.04	>90 %			
This work	Abs	1.8768	>99.9 %	30	Graphene & VO_2	5
	PC	2.12–3.58	>90 %			

Abbreviations: Abs — absorption; PC — polarization conversion; A — absorbance; PCR — polarization conversion ratio.

parameters, the incident angle as well as the polarization angle on the performance of the two functions. The proposed metasurface has the advantages of switchable functions and simple structure compared to some other reported results, which makes it have potential applications in terahertz absorption, polarization conversion, modulation, and imaging.

CRediT authorship contribution statement

Xuejun Lian: Conceptualization, Visualization, Software, Investigation, Writing - original draft. Mengting Ma: Conceptualization, Visualization, Software, Investigation.

Jinping Tian: Methodology, Validation, Formal analysis, Software, Writing - review & editing. Rongcao Yang: Formal analysis, Review & editing.

Declaration of competing interest

The authors declare that they have no known competing financial interests or personal relationships that could have appeared to influence the work reported in this paper.

Data availability

Data will be made available on request.

Acknowledgements

This work was supported the National Natural Science Foundation of China (Grants No. 61775126). We are grateful to the anonymous reviewers for their valuable and constructive suggestions on this paper, which have greatly helped us improve the entire discussion.

References

[1] Z.H. Liu, X.J. Li, J. Yin, Z. Hong, Asymmetric all silicon micro-antenna array for high angle beam bending in terahertz band, IEEE Photon. J. 11 (2) (2019) 5900509.

[2] R. Kargar, K. Rouhi, A. Abdolali, Reprogrammable multifocal THz metalens based on metal-insulator transition of VO_2-assisted digital metasurface, Opt. Commun. 462 (2020), 125331.

[3] H.Y. Sun, L. Zhao, J.S. Dai, Y.Y. Liang, J.P. Guo, H.Y. Meng, H.Z. Liu, Q.F. Dai, Z. C. Wei, Broadband filter and adjustable extinction ratio modulator based on metal-graphene hybrid metamaterials, Nanomaterials 10 (7) (2020) 1359.

[4] J.B. Brückner, J. Le Rouzo, L. Escoubas, G. Berginc, O. Calvo-Perez, N. Vukadinovic, F. Flory, Metamaterial filters at optical-infrared frequencies, Opt. Express 21 (14) (2013) 16992–17006.

[5] Z.H. Chen, H. Chen, J.K. Yin, R.Y. Zhang, H. Jile, D.Y. Xu, Z. Yi, Z.G. Zhou, S.S. Cai, P.G. Yan, Multi-band, tunable, high figure of merit, high sensitivity single-layer patterned graphene-perfect absorber based on surface plasmon resonance, Diam. Relat. Mater. 116 (2021), 108393.

[6] Y.J. Yuan, Y.P. Qi, B.H. Zhang, J.H. Ding, W.M. Liu, H.W. Chen, X.X. Wang, A polarization-insensitive, wide-angle dual-band tunable graphene metamaterial perfect absorber with T-shaped strips and square ring, Phys. Scr. 97 (2) (2022), 025507.

[7] F.Y. Yu, X.J. Shang, W. Fang, Q.Q. Zhang, Y. Wu, W. Zhao, J.F. Liu, Q.Q. Song, C. Wang, J.B. Zhu, X.B. Shen, A terahertz tunable metamaterial reflective polarization converter based on vanadium oxide film, Plasmonics 17 (2) (2022) 823–829.

[8] Y.Y. Jiang, M. Zhang, W.H. Wang, Z.Y. Song, Reflective and transmissive cross-polarization converter for terahertz wave in a switchable metamaterial, Phys. Scr. 97 (1) (2022), 015501.

[9] Y.H. Sun, Y. Wang, H. Ye, J. Li, H.J. Fan, L. Yu, Z.Y. Yu, Y.M. Liu, T.S. Wu, Switchable bifunctional metasurface based on VO_2 for ultra-broadband polarization conversion and perfect absorption in same infrared waveband, Opt. Commun. 503 (2022), 127442.

[10] J.L. He, Q.H. Zhu, Y.J. Zhou, J.J. Wang, G.F. Cai, M.H. Li, J.F. Dong, Lightweight switchable bifunctional metasurface based on VO_2: high-efficiency absorption and ultra-wideband circular polarization conversion, Optik 257 (2022), 168837.

[11] Z.Z. Wu, J.P. Tian, R.C. Yang, A graphene based dual-band metamaterial absorber for TE polarized THz wave, Micro Nanostruct. 168 (2022), 207331.

[12] F.Y. Yu, J.B. Zhu, X.B. Shen, Tunable and reflective polarization converter based on single-layer vanadium dioxide-integrated metasurface in terahertz region, Opt. Mater. 123 (2022), 111745.

[13] R.X. Wang, L. Li, J.L. Liu, F. Yan, F.J. Tian, H. Tian, J.Z. Zhang, W.M. Sun, Triple-band tunable perfect terahertz metamaterial absorber with liquid crystal, Opt. Express 25 (26) (2017) 32280–32289.

[14] W. Liu, Y.S. Lv, J.P. Tian, R.C. Yang, A compact metamaterial broadband THz absorber consists of graphene crosses with different sizes, Superlattice. Microst. 159 (2021), 107038.

[15] D.W. Yu, Y.F. Dong, Y.D. Ruan, G.C. Li, G.S. Li, H.M. Ma, S. Deng, Z.P. Liu, Photo-excited switchable terahertz metamaterial polarization converter/absorber, Crystals 11 (9) (2021) 1116.

[16] J.Y. Wang, R.C. Yang, R.B. Ma, J.P. Tian, W.M. Zhang, Reconfigurable multifunctional metasurface for broadband polarization conversion and perfect absorption, IEEE Access 8 (2020) 105815–105823.

[17] Y.R. Li, J. Luo, X. Li, M.B. Pu, X.L. Ma, X. Xie, J.P. Shi, X.G. Luo, Switchable quarter-wave plate and half-wave plate based on phase-change metasurface, IEEE Photon. J. 12 (2) (2020) 4600410.

[18] H.Y. Zhang, C.H. Yang, M. Liu, Y.P. Zhang, Dual-function tunable asymmetric transmission and polarization converter in terahertz region, Results Phys. 25 (2021), 104242.

[19] H.R. He, X.J. Shang, L. Xu, J.J. Zhao, W.Y. Cai, J. Wang, C.J. Zhao, L.L. Wang, Thermally switchable bifunctional plasmonic metasurface for perfect absorption and polarization conversion based on VO_2, Opt. Express 28 (4) (2020) 4563–4570.

[20] J.S. Li, X.J. Li, Switchable tri-function terahertz metasurface based on polarization vanadium dioxide and photosensitive silicon, Opt. Express 30 (8) (2022) 12823–12834.

[21] Z.X. Su, J.B. Yin, X.P. Zhao, Terahertz dual-band metamaterial absorber based on graphene/MgF_2 multilayer structures, Opt. Express 23 (2) (2015) 1679–1690.

[22] M. Zhang, J.H. Zhang, A.P. Chen, Z.Y. Song, Vanadium dioxide-based bifunctional metamaterial for terahertz waves, IEEE Photon. J. 12 (1) (2020) 4600109.

[23] M. Zhang, Z.Y. Song, Terahertz bifunctional absorber based on a graphene-spacer-vanadium dioxide-spacer-metal configuration, Opt. Express 28 (8) (2020) 11780–11788.

[24] Z.Y. Song, A.P. Chen, J.H. Zhang, Terahertz switching between broadband absorption and narrowband absorption, Opt. Express 28 (2) (2020) 2037–2044.

[25] W.W. Liu, J.S. Xu, Z.Y. Song, Bifunctional terahertz modulator for beam steering and broadband absorption based on a hybrid structure of graphene and vanadium dioxide, Opt. Express 29 (15) (2021) 23331–23340.

[26] A. Norouzi-Razani, P. Rezaei, Broadband polarization insensitive and tunable terahertz metamaterial perfect absorber based on the graphene disk and square ribbon, Micro Nanostruct. 163 (2022), 107153.

[27] Y.J. Zhao, R.C. Yang, J.Y. Wang, X. Wei, J.P. Tian, W.M. Zhang, Dual-mode terahertz broadband polarization conversion metasurface with integrated graphene-VO_2, Opt. Commun. 510 (2022), 127895.

[28] Z.K. Zhou, Z.Y. Song, Terahertz mode switching of spin reflection and vortex beams based on graphene metasurfaces, Opt. Laser Technol. 153 (2022), 108278.

[29] C.H. He, Z.Y. Song, Terahertz graphene metasurfaces for cross-polarized deflection, focusing, and orbital angular momentum, Opt. Express 30 (14) (2022) 25498–25508.

[30] C.Q. Li, Z.Y. Song, Tailoring terahertz wavefront with state switching in VO_2 Pancharatnam–Berry metasurfaces, Opt. Laser Technol. 157 (2023), 108764.

[31] R.X. Nie, C.H. He, R.X. Zhang, Z.Y. Song, Vanadium dioxide-based terahertz metasurfaces for manipulating wavefronts with switchable polarization, Opt. Laser Technol. 159 (2023), 109010.

[32] H.L. Zhu, Y. Zhang, L.F. Ye, Y.K. Li, Y.H. Xu, R.M. Xu, Switchable and tunable terahertz metamaterial absorber with broadband and multi-band absorption, Opt. Express 28 (26) (2020) 38626–38637.

[33] J. Li, C.L. Zheng, J.T. Li, H.L. Zhao, X.R. Hao, H. Xu, Z. Yue, Y.T. Zhang, J.Q. Yao, Polarization-dependent and tunable absorption of terahertz waves based on anisotropic metasurfaces, Opt. Express 29 (3) (2021) 3284–3295.

[34] D.X. Yan, M. Meng, J.S. Li, J.N. Li, X.J. Li, Vanadium dioxide-assisted broadband absorption and linear-to-circular polarization conversion based on a single metasurface design for the terahertz wave, Opt. Express 28 (20) (2020) 29843–29854.

[35] Z.Y. Xiao, H.L. Zou, X.X. Zheng, X.Y. Ling, L. Wang, A tunable reflective polarization converter based on hybrid metamaterial, Opt. Quant. Electron. 49 (12) (2017) 401.

[36] Z.Y. Song, A.P. Chen, J.H. Zhang, J.Y. Wang, Integrated metamaterial with functionalities of absorption and electromagnetically induced transparency, Opt. Express 27 (18) (2019) 25196–25204.

[37] J.X. Zhao, J.L. Song, Y. Zhou, Y.C. Liu, J.H. Zhou, Switching between the functions of half-wave plate and quarter-wave plate simply by using a vanadium dioxide film in a terahertz metamaterial, Chin. Phys. Lett. 37 (6) (2020), 064204.

[38] Y.S. Lv, W. Liu, J.P. Tian, R.C. Yang, Broadband terahertz metamaterial absorber and modulator based on hybrid graphene-gold pattern, Phys. E Low-dim. Syst. Nanostruct. 140 (2022), 115142.

[39] Y.J. Zhao, R.C. Yang, Y.X. Wang, W.M. Zhang, J.P. Tian, VO_2-assisted multifunctional metamaterial for polarization conversion and asymmetric transmission, Opt. Express 30 (15) (2022) 27407–27417.

[40] Z.H. Li, R.C. Yang, J.Y. Wang, Y.J. Zhao, J.P. Tian, W.M. Zhang, Multifunctional metasurface for broadband absorption, linear and circular polarization conversions, Optic. Mater. Exp. 11 (10) (2021) 3507–3519.

[41] M.S. Islam, J. Sultana, M. Biabanifard, Z. Vafapour, M.J. Nine, A. Dinovitser, C.M. B. Cordeiro, B.W.H. Ng, D. Abbott, Tunable localized surface plasmon graphene metasurface for multiband super-absorption and terahertz sensing, Carbon 158 (2020) 559–567.

[42] Z.Y. Song, J.H. Zhang, Achieving broadband absorption and polarization conversion with a vanadium dioxide metasurface in the same terahertz frequencies, Opt. Express 28 (8) (2020) 12487–12497.

[43] H.T. Chen, Interference theory of metamaterial perfect absorbers, Opt. Express 20 (7) (2012) 7165–7172.

[44] X. Gao, X. Han, W.P. Cao, H.O. Li, H.F. Ma, T.J. Cui, Ultrawideband and high-efficiency linear polarization converter based on double V-shaped metasurface, IEEE Trans. Antennas Propag. 63 (8) (2015) 3522–3530.

[45] M.Q. Zou, M.Y. Su, H. Yu, Ultra-broadband and wide-angle terahertz polarization converter based on symmetrical anchor-shaped metamaterial, Opt. Mater. 107 (2020), 110062.

[46] Y.J. Liu, H.L. Yang, X.J. Huang, Z.T. Yu, S.R. Li, Y.J. Yang, A metamaterial polarization converter with half reflection and half transmission simultaneously, Phys. Lett. A 389 (2021), 127101.

[47] K. Liao, S.B. Liu, X.Y. Zheng, X.W. Zhang, X.X. Shao, X.K. Kong, Z.Y. Hao, A polarization converter with single-band linear-to-linear and dual-band linear-to-circular based on single-layer reflective metasurface, Int. J. RF Microw. Comput.-Aided Eng. 32 (2) (2022), e22955.